

Deposition of ultra-thin coatings by a nature-inspired Spray-on-Screen technology

Rachith nithyananda kumar (✉ rachith.shanivarasanthe@uhasselt.be)

Hasselt University

Andrea Rameirez

IMO-IMOMEC, U Hasselt

Pieter verding

IMO-IMOMEC, U Hasselt

Philippe Nivelles

IMO-IMOMEC, U Hasselt

Frank Renner

IMO-IMOMEC, U Hasselt <https://orcid.org/0000-0003-0425-393X>

Jan D'Haen

IMO-IMOMEC, U Hasselt <https://orcid.org/0000-0003-4487-3885>

Wim Deferme

IMO-IMOMEC, U Hasselt <https://orcid.org/0000-0002-8982-959X>

Article

Keywords: dynamic wetting, ultra thin films, spray on screen, surface roughness, nanoparticles, large area deposition

Posted Date: October 27th, 2022

DOI: <https://doi.org/10.21203/rs.3.rs-2061871/v1>

License: © ⓘ This work is licensed under a Creative Commons Attribution 4.0 International License. [Read Full License](#)

Version of Record: A version of this preprint was published at Communications Engineering on June 22nd, 2023. See the published version at <https://doi.org/10.1038/s44172-023-00093-0>.

Abstract

Nanometer-thick, ultrathin coatings applied over a large area are of paramount importance for various application fields such as biomedicine, space and automotive, organic electronics, memory devices, or energy storage devices. So far wet chemical deposition as a cost-effective, scalable, and versatile method can only be used for thicker deposits. Here the formation of uniform ultra-thin coatings with thicknesses below 15nm using a nature-inspired, roll-to-roll compatible Spray-on-Screen (SoS) technology is reported. For this, the finite micro-droplet generation of Ultrasonic Spray Coating (USSC) is combined with the coating formation from a screen printing mesh. Hydrophobic micro-threads of the mesh, resembling the micro-hair on the legs of water striders, produce millidroplets from microdroplets, and when applying external pressure to the mesh, dynamic wetting is enforced. The proposed technology is applicable for a wide variety of substrates and applications. It is shown by theory and experiment that ultra-thin coatings below 5nm homogeneous over a large area can be deposited without the use of extended ink formulation or high substrate temperatures during or after deposition. This simple yet effective technique enables the deposition of ultra-thin films on any substrates, and is very promising to fabricate the organic, inorganic electronics devices and batteries cost effectively.

Introduction

Growing research on ultra-thin coatings is essential due to its diverse field of applications which includes biocompatible coatings¹ in biomedical devices, ultra-low friction and wear-resistant thin films in space and automotive fields,² functional thin coatings in thermoelectric³, photovoltaics⁴, light-emitting diodes⁵, sensors⁶, spintronics⁷, lasers⁸, batteries⁹, super capacitors¹⁰ etc. Conventionally, fabrication of these thin coatings includes expensive and time-consuming vacuum deposition techniques like sputtering¹¹, thermal¹² and e-beam evaporation¹³, atomic layer deposition¹⁴, molecular beam epitaxy¹⁵, metal-organic chemical vapour deposition¹⁶ etc. Solution processable techniques like spin coating¹⁷ offer a unique solution of achieving uniform thin coatings¹⁸ at a low cost. Spin coating however has one major disadvantage: it lacks the capability of upscaling to big areas. Other solution processing techniques like dip-coating¹⁹, inkjet printing^{20,21}, slot-die coating²², doctor blade coating²³, screen printing²⁴, spray coating²⁵, spray pyrolysis²⁶ are roll-to-roll (R2R) compatible but they are incapable of depositing ultra-thin coatings (< 15 nm) without extended ink formulation or heat treatments²⁰, which is not suitable for temperature-sensitive substrates. In **(Figure S1)**, different solution processing techniques are depicted showing the relationship between scalability and minimal layer thickness as described in the literature. Droplet-based technologies such as inkjet printing and spray coating need an optimized ink formulation and a thermal heat treatment to achieve ultra-thin coatings and have the problem of coffee rings and Marangoni flow²⁷. Depositing droplets on surfaces leads to a inhomogeneous surface coverage by the coffee ring²⁸ effect. If the droplets are larger than the capillary length, then gravity dominates the wetting behaviour and might deform the soft substrates. If not, (microdroplets), then the surface tension of the liquid dominates which would hinders the nature of wetting. However, the latter could be overcome by forced dynamic wetting, which could allow partial wetting of the liquid to spread uniformly over the substrate and this occurs when the liquid velocity is set by an external force, unlike the equilibrium wetting induced by the capillary force²⁹. Since the microdroplets evaporate very fast (~ 30 ms)^{30,31}, by the time an external force is being applied to initiate the dynamic wetting, the droplets would evaporate and

again form coffee rings. Therefore, instead of depositing a microdroplet directly on the substrate, if in case a thin film of liquid is deposited, then by dynamic wetting, the influence of the coffee rings and hence the irregular deposition could be eliminated. Therefore, we establish that to achieve a uniform thin film we should have a simultaneous effect of generating a uniform thin film over the substrate, and to apply the external force to activate dynamic wetting and this brings about an additional challenge.

Also here, nature has its example: water striders are water-walking insects thanks to their non-wetting legs³²⁻³⁴. These legs are covered with a large number of tiny hair³⁵ as shown in (**Figure S2**). Each of these tiny hairs have nano-grooves to possess water resistance. Due to this unique combination of hierarchical micro and nanostructure on the legs surface, the dimples created by the legs on the water can be up to $4.38 \pm 0.02\text{mm}$ in depth, without piercing the water, which is significantly greater than the capillary length of water $\sim 2.7\text{mm}$ ³⁵. Therefore, a combination of hierarchical microstructure could shear the liquid without piercing. This ingenious technology in nature has inspired us to use non-wetting microstructures for a dual purpose: 1) convert the microdroplets into milli-droplets (microdroplet coalescence) and 2) induce dynamic wetting of the liquid, without breaking the surface of the liquid. Hence, a uniform spreading of the thin liquid film over the substrate thereby results in the formation of a uniform ultra-thin coating of the selected material over any given substrate.

After a theoretical introduction on the Spray-on-Screen technology (SoS), this article will show the deposition of ultrathin coatings with the SoS technology measuring the thickness and roughness of the final coatings. For a water based poly(3,4-ethylenedioxythiophene) polystyrene sulfonate (PEDOT:PSS) formulation, isopropanol alcohol (IPA) based polyethylenimine, 80% ethoxylated (PEIE) ink and IPA based Zinc oxide (ZnO) nanoparticle formulation, we achieved the thickness of 15.8nm, 4.8nm and 15.3nm respectively with surface roughness (RMS) of 1.1nm, 0.3nm and 2.6nm respectively. The unique combination of droplet generation with Ultrasonic spray coating (USSC), the microdroplet coalescence and the dynamic wetting applying a screen printing mesh, mimicking nature, results in ultra-thin ($< 15\text{nm}$), homogeneous coatings for large area deposition, to our knowledge never shown before in the scientific literature.

Spray-on-Screen coating technology

To realize the idea of using nature-inspired forced dynamic wetting of the microdroplets on any substrate, we have used USSC for the generation of microdroplets (Fig. 1b), and a screen mesh to convert the microdroplets to milli-droplets (due to its microstructure) and to facilitate the forced dynamic wetting of the deposited liquid (Fig. 1a, d). We stipulate that this thin film could best be formed above the substrate (thus on the screen mesh) to prevent the evaporation and thus coffee ring formation on the substrate itself.

The selection of USSC is mainly due to the capability of forming homogeneous droplets less than $100\text{ }\mu\text{m}$ in diameter (Fig. 1c, and **Supplementary video 1**). Further, the velocity of the generated droplets can be easily controlled by the nitrogen pressure, reducing the singularity which exists for other spray coating technologies; i.e. velocity and/or temperature-induced droplet interaction with the mesh of the screen³⁶. Details of the working of USSC is given in the supplementary information **S 1**. A polyester mesh, as can be seen from the SEM image in (Fig. 1e), is typically applied for screen printing, with a dimension of the thickness of the wire (t) $\sim 50\text{ }\mu\text{m}$ and the interspacing between the wires (w) $\sim 40\text{ }\mu\text{m}$ was used for a dual purpose: to convert the

microdroplets into milli-droplets and to facilitate the forced dynamic wetting of the deposited liquid as is explained in more detail before. Inset of Fig. 1e shows the hydrophobic nature of the polyester mesh, which mimics the water striders leg, where it allows for the forced dynamic wetting without piercing the liquid of interest. The polyester screen mesh was cleaned thoroughly (details of cleaning is given in materials and methods) before the conduction of the experiments and possessed an equilibrium water contact angle of 104.6 ° (**Figure S3**). The present mesh could be considered as a substrate with textures. As explained by Marmur *et al.*³⁷ the wetting on a rough surface (or in our case textured substrate) assumes multiple local free energy minima with different contact angles. Finally, the overall free energy minima could follow the traditional contact angle theory values once the droplet is much larger than the roughness scale of the substrate underneath. Also, since the periodic textures on the surface involve multiple pinning points, there would be multiple local minima of free energy and hence the obtained water contact angle is different from the substrate made up of polyester without any texture. However, this analysis would be entirely different for the droplet whose dimensions are less than the capillary length and as in our case equal or smaller than the throat (w) of the mesh. In here, the four corners of the mesh act as individual pinning points and act as local minima of free energy. Also, in our case, the pressure exerted by the nitrogen gas upon the droplets makes the analysis of free energy a complex phenomenon. Therefore, understanding of the global free energy minima to attain the equilibrium is a complicated state of affair. In the following section we explain the process of reaching the global minima on the mesh and the process of forced dynamic wetting by the mesh.

Theoretical and experimental approach for the technology

2.1. Theoretical approach for the ultra-thin film deposition.

As thousands of droplets are being generated by USSC hitting the mesh within the same time frame, these micro-droplets coalesce before they evaporate and form milli-droplets (**Figure S4**). The formation and profile of the milli-droplets upon coalescence of microdroplets depends on the spreading coefficient and the geometry of the surface texture. The spreading coefficient (S) is usually calculated to distinguish between different wetting states (Eq. 1). In general, it represents the surface energy difference between partial and complete wetting stages (Fig. 2g), i.e. at partial wetting, θ would be in between 90° and 180° and at complete wetting, θ would be 180°. Therefore:

$$S = \gamma_{sv} - (\gamma_{sl} + \gamma_{lv})$$

1

Where, γ_{sl} , γ_{sv} and γ_{lv} are the surface tension at solid/liquid, solid/vapor and liquid/vapor region respectively. If the spreading coefficient is equal to or more than zero, then the droplet completely wets the surface and if it is less than zero then the droplet partially wets the surface. Based on the surface tension of the formulation and the surface energy of the mesh material, S can be determined. In the present work, a low surface energy polyester mesh (43 mN m⁻¹)³⁹ and two different formulations at opposite ends of the surface tension spectrum were studied.

For water as a solvent ($\gamma = 72 \text{ mN m}^{-1}$), being a high surface tension liquid, water would inevitably result in partial wetting. Therefore, there could be two situations, a) the deposited microdroplets would coalesce into a

sizable hemispherical milli-droplet, b) the microdroplets would be pushed towards the downside of the mesh by the applied nitrogen pressure. The latter would happen only if the diameter of the droplet is smaller than the throat area of the mesh. The former resembles the drop sitting on top of air pockets and the growth and profile of the droplet are dominated by the roughness of the surface texture. In this case, (Fig. 2d, **inset top right** of Fig. 2e), where a drop is sitting on top of the pockets, the contact angle relation is given by the Cassie-Baxter model (Fig. 2d) $\cos(\theta^*) = r \varphi_s \cos(\theta_E) - (1 - \varphi_s)$, where $(1 - \varphi_s)$ is the area made by the liquid-air fraction. As $\varphi_s \geq 0$ the apparent contact angle $\theta^* \geq 180^\circ$ even for a surface whose $\theta_E < 90^\circ$.

On the other hand, for a low surface tension liquid like isopropanol alcohol (22 mN m^{-1}), wetting would be complete; i.e. it will completely wet the threads of the mesh. Any further deposition would result in increasing the thickness of the deposited droplet on the mesh's thread, which grows until the droplet from two neighbouring mesh threads reach the critical thickness ($w/2$, w is the width of the throat of the mesh) wherein coalescence would result in a continuous liquid film between the mesh. Upon further deposition of the microdroplets, the continuous thin film between the mesh would keep spreading over the neighbour thread of the mesh and simultaneously grow both in width and thickness. The milli-droplet would acquire the hemispherical shape, with the top half being above the mesh and the bottom half being below the mesh (droop R_d), as is shown in (Fig. 2b, **inset top right**). The curvature of the droplet is governed by the Laplace equation and the curvature is the same on the top and bottom of the mesh^{36,43}. The Laplace equation relates the pressure inside the droplet to its curvature. Further increase in droplet deposition increases the width and thickness of the coagulated droplet until it reaches the capillary length. For the fully wetted state, like for the case of IPA wetting on the mesh (liquid of low surface tension), (Fig. 2a), the relationship between the apparent or macroscopic contact angle (θ^*) and the equilibrium contact angle (θ_E) of a smooth flat substrate is given by the Wenzel Eq. 4⁴, $\cos(\theta^*) = r \cos(\theta_E)$, where r is the roughness parameter that describes the ratio between the actual area wetted by the liquid (including the pores) to the area projected onto a flat substrate. Therefore, the spread-ability of the deposited liquid over the mesh depends on the surface tension of the solvent being used.

Since the spreading coefficient predicts the state of wetting, we tried to understand this by dropping a microliter droplet ($2 \mu\text{l}$) on the mesh and followed the wettability of the droplet over the mesh. Depending on the surface tension of the liquid, the wetting behaviour on the mesh is altered. As can be seen from (Fig. 2b, **and inset top right**), the low surface tension liquid IPA completely wets the mesh (hydrophilic) and liquid droops down the mesh achieving the same length, thickness and curvature as the liquid on top of the mesh, (Fig. 2c **and inset top right**) (zoomed bottom image showing the complete wetting of thread by IPA). If a substrate is placed underneath the mesh between, $0 \geq x$, the droplet touches the substrate. Here x is the distance between the substrate and the bottom of the droplet, R_d is the droplet diameter and D is the thickness of the mesh.

With water as a solvent, as seen in (Fig. 2e **and inset top right**), the hydrophobic behaviour is exhibited. This could be seen as a droplet sitting on air pockets, which resembles the Cassie-Baxter state of wetting, (Fig. 2d). Water forms a meniscus around the thread, (Fig. 2 **and inset top right**). At equilibrium, the maximum droop of the droplet would be at the centre of the mesh opening, with a droop length of $\delta = (\sqrt{2} P D)^2 / 8 R_d$ ³⁶ where, R_d is the radius of the droplet, D is the thickness of the mesh and P is the pitch. The droop of water for a 1-millimetre diameter droplet could be seen in (Fig. 2f). As the droplet diameter reduces, the droop length

increases. If finally, δ becomes greater than $D/2$, then the droplet touches the substrate underneath the mesh, (Fig. 2f and inset top right).

Even as the solvents being used are at the opposite end of surface tension, once the droplet touches the substrate, there exist two situations that come to light once the drooped liquid on screen touches the bottom substrate: The first situation is where, the capillary force that arose between the substrate, the liquid on the mesh and the air interface would result in the spreading of the liquid onto the substrate to reach the global minimum of the substrate's surface energy. This initiates a hydrodynamic flow of the droplet⁴⁷. Once the thin liquid film formed on the mesh touches the bottom substrate, the liquid will be drawn from the thin film and would form a meniscus between the mesh and the substrate (inset Fig. 2, c and f). An attractive force is generated by the formed meniscus. The attractive force is mainly due to the existence of the surface tension of the liquid around the periphery of the meniscus and due to the reduced pressure inside the meniscus as compared to the capillary pressure. This attractive force results in the second situation where attractive force pulls the mesh towards the substrate and drains the liquid above the mesh. By assuming the height of the meniscus m_h to be smaller than the capillary length l_c , the capillary force (F) is given by (Equation. 2)⁴⁷ and it can be seen in Fig. 2h,

$$F = 2\pi\gamma R_d \left(2c - \frac{x}{m_r} \right)$$

2

where γ is the surface tension of the liquid, R_d is the droplet radius, β is the filling angle, Φ_1 and Φ_2 are the contact angle of the liquid meniscus with the drooped liquid and with the substrate respectively, x is the distance between the drooped liquid and substrate and constant c can be calculated from the Eq. 3, which is given by:

$$c = \frac{\cos(\beta + \Phi_1) + \cos(\Phi_2)}{2}$$

3

This force created would then be applied by the screen mesh on the fluid which influences the wetting behaviour and hence forced dynamic wetting will happen. Also, as there would be many milli-droplets formed due to the microdroplets, these individual droplets would simultaneously try to wet the substrate (Fig. 1d). Finally, these multiple droplets will form a coating with an abrupt increase in the amplitude of the coating thickness when the droplets deposited on the screen interfere constructively in the substrate. Fortunately, the presence of the screen mesh prevents the formation of abrupt thin liquid coatings, due to the applied force by the screen mesh over the liquid film, which resembles the force exerted by the nano-hairs of the water striders on a liquid. The hydrostatic pressure inside the liquid increases, which forces the liquid to flow in lateral dimensions. This induces dynamic wetting, which follows the hydrodynamic flow induced by the capillary force. The combination of capillary force and the external force applied by the mesh would assure that the liquid wets the surface irrespective of the solvent and type of substrate being used.

2.2 Experimental approach for the ultra-thin film deposition.

To corroborate the flexibility of the SoS on the formation of ultra-thin coatings, PEDOT:PSS, a water based material, 1:10 by volume, PEIE in IPA, 0.1:35 by volume, and a polymer-metal oxide composite of ZnO nanoparticles with a diameter of 10-15nm mixed with PEIE in IPA as a solvent, 1:0.1:35 by volume, is deposited on Indium Tin Oxide substrates (ITO). ITO substrates with a size of $2.5 \times 2.5 \text{ cm}^2$ in size are cleaned according to the cleaning protocol given in material and methods and UV-treated for 30 min before being deposited by the formulation of interest. The surface energy of the ITO is measured and calculated by using Fowke's theory⁴⁸, and it was found to be 117.37 mN m^{-1} . The obtained results are compared with standard spin-coated layers of the same materials on ITO substrates.

The deposition conditions for all three cases are given in Table 1. The distance between the substrate and the nozzle of the USSC and the room temperature is kept constant for all sets of experiments at 6 cm and 22°C respectively. And the distance between the screen mesh and the substrate is kept above the droop length of both the solvents, i.e. at 140µm. Upon the deposition of droplets on the screen, the screen is made to touch the substrate so that the capillary force would draw the liquid from the top of the screen and would induce forced dynamic wetting. It should be noted that the mesh, which is held by capillary force, should be released from the substrate otherwise the deposited material would be deposited only at the region where the mesh thread overpassing takes place (**Figure S6**).

Table 1
Deposition parameters for the various materials and the solvents used

	Substrate temp ° C	Solution concertation	Number of passes	Nitrogen pressure	Flow rate ml min ⁻¹	Path speed mm s ⁻¹
PEDOT:PSS	60	1 ml PEDOT:PSS/15 ml water	1	1.5 kPa	0.5	10
PEIE	30	0.01 ml in 30 ml IPA	1	1.5 kPa	0.8	10
ZnO + PEIE	30	2 ml ZnO + 0.01 ml PEIE + 50 ml IPA	1	1.5 kPa	0.9	10

To begin with, the uniformity of the deposited layers over the large area is investigated by optical microscopy and as is clearly seen from (Fig. 3, a,b and **c**), irrespective of the materials and solvents being used, the deposited layers show a uniform deposition without any coffee rings. Because of the absence of irregularities in the thickness of the deposited coating over a large area, this technique promises a new regime of upscalable fabrication technology for ultra-thin films, provided the obtained thickness is less than 15nm.

To determine the thickness of the different materials, tapping mode AFM is applied⁴⁹ and the sequence of measuring the thickness by AFM is given in the Fig. 3o and in supplementary information **S 10–12**. As an example in Fig. 3m and n, the measured thickness which is calculated by utilizing the profile over the scratch 10 times is shown for PEIE deposited on small ($2.5 \times 2.5 \text{ cm}^2$) and large substrates ($5 \times 5 \text{ cm}^2$) respectively. To measure the thickness, all materials are deposited on ITO coated glass slides and the concentration of the solution is varied by keeping all other parameters constant. The desired ultra-low thickness of the material of

interest was achieved by varying the solution concentration and the flow rate of the solution. PEDOT:PSS being diluted in water evaporated less during the flight from the nozzle to the screen and hence the flow rate was less compared to IPA based materials (Table 1). Also to evaporate the deposited thin liquid film for PEDOT:PSS, the substrate temperature was kept at 60°C, which is also more than the substrate temperature used for IPA based materials, which was 30°C. Excess of solution flow rate resulted in an edge effect^{50,51}, where more material was accumulated. Therefore, the flow rate was optimized according to the evaporative properties of the solvent being used. The minimum thickness achieved for PEDOT:PSS, PEIE and ZnO-PEIE is $15.8 \pm 0.6\text{nm}$, $4.8 \pm 0.1\text{nm}$ and $15.3 \pm 0.6\text{nm}$ respectively, as is shown in Table 2. To further investigate the effect of solution concentration on the thickness of the deposited coatings, a comprehensive investigation was done for all three materials with varying concentrations and the results are shown in (Table S1). The obtained results show that by varying the concentration of the solvent, the thickness of the deposited layer could be varied. The surface roughness (RMS) of the PEDOT:PSS, PEIE and ZnO-PEIE composite thin coating deposited on the ITO substrate is found to be around 1.1nm, 0.3nm and 2.6nm respectively, which can be seen in (Fig. 3, d, e and f). These obtained surface roughnesses are comparable with the spin coated devices (Figure S 7, 8 and 9). This clearly shows that the Spray-on-Screen deposition has the same surface morphological properties as that of spin coated devices. Therefore, by achieving ultra-low thickness and very low surface roughness of the deposited film, this technology has filled the gap which was exciting in the upscalability of ultra-thin coating fabrication, potentially exhibiting a paradigm shift in the ultra-thin film market.

Table 2
Minimum thickness achieved for the different materials over the ITO substrate

	PEDOT:PSS	PEIE	ZnO + PEIE
Minimum Thickness	$15.8 \pm 0.6\text{nm}$	$4.8 \pm 0.1\text{nm}$	$15.3 \pm 0.6\text{nm}$
Surface roughness (RMS)	1.1nm	0.36nm	2.6nm

However, the previous results have been demonstrated on a high surface energy substrate like ITO, the SoS does not render itself as the ultimate fabrication technology unless it shows its versatility on a low surface energy substrate. Therefore, to investigate the flexibility of SoS, low surface energy, temperature sensitive super yellow (SY) light emitting PPV copolymer is used as a substrate. The surface energy of the super yellow is measured by using Fowke’s theory, which is around 56 mN m^{-1} . The details of measurements are given in the supplementary information S-5. The materials and the deposition conditions used in the previous studies on ITO are being duplicated on the SY substrates. AFM measurements were performed to measure the surface morphology of the deposited PEDOT:PSS, PEIE and ZnO-PEIE composite. The obtained results are shown in (Fig. 3, g, h and i). The surface roughness (RMS) of the deposited films was 1.1nm, 0.8nm and 2.6nm respectively for PEDOT:PSS, PEIE and ZnO-PEIE composite, which is almost similar to the results obtained for the films deposited on the ITO substrate. SEM images obtained on the same set of samples also confirm that there are no coffee rings and the film is uniform throughout (Fig. 3, j, k and l), even though the super yellow substrate was of low surface energy and soft (15.54 MPa, Supplementary information 15–17 and Figure S17). This extraordinary result confirms the independence of the Spray-on-Screen technology on the nature of the

substrate. Finally, we demonstrate that this innovative Spray-on-Screen technology is perfectly suited for upscaling. Therefore, a larger $5 \times 5 \text{ cm}^2$ sample was coated with PEIE, the thickness and the surface roughness of the film is measured. A thickness of 5.9nm (Fig. 3n) and surface roughness (RMS) of 0.9nm was achieved, and these obtained values are the same as for the small devices. The movie for the SoS is attached in the supplementary information (**supplementary video S2**). To clearly visualize the conversion of microdroplets into milli droplets on the screen mesh, a darker formulation of PEDOT:PSS is shown in the (**supplementary video S2**). As can be seen clearly from the movie, the proposed Spray-on-Screen works well for larger samples as well. This demonstrates the upscale-ability of the Spray-on-Screen technology over large samples.

To display the suitability of the SoS to deposit ultrathin films on large areas, we demonstrate the deposition of an organic light emitting diode (OLED) as a potential application case, amongst many other that can be achieved with this innovative SoS technology. The methods of fabricating and characterizing the OLEDs are given in supplementary information S18. Since the OLED performance is highly dependent on the thickness of the various layers used, the ultrathin layer herein used is the electron injection layer (EIL). For the present case, the state-of-the-art standard device consisting of calcium as EIL deposited by thermal evaporation and also ZnO-PEIE nanocomposite as an EIL built by spin coating is compared with the SoS coated ZnO-PEIE nanocomposite. The thickness of this layer is well below 30nm and therefore only vacuum deposition and spin coating are possible deposition techniques, apart from our SoS technology. In view of upscaling and ease of production, spin coating (only for small scale) and vacuum deposition (in need of high vacuum systems) are replaced here by the innovative Spray-on-Screen technology, capable of depositing the large area, ultrathin coatings with the ease of production of wet chemical solution processing. The structure of the solution processed materials is shown in Fig. 4(a) with their chemical structure in Figs. 4(b),(c) and (d) respectively. A slight variation in the thickness of the EIL would result in adversely affecting the OLED performance and the non-homogeneous layers, pinholes would manifest as dark spots in the illuminated devices and also, the thicker HTL or EIL would influence the electroluminescence (EL) curve due to the cavity effect. As visible from Fig. 4(e), the max EL peak for all the devices is $\sim 554 \text{ nm}$, this confirms the thickness of the SoS deposited PEDOT:PSS and ZnO + PEIE nanocomposite is the same as the spin coated ones. The top inset of Fig. 4(e) shows the illuminated small area OLEDs with SoS deposited HTL and EIL. The presence of microparticles, i.e. impurities, would create a short pathway for the charges to flow and induce dark spots, however as seen from the bottom inset of Fig. 4(e), the illumination is constant throughout. The OLED performance parameters like J-V-L and EQE-V-Luminous efficacy characteristics of the device built by SoS HTL and EIL exhibit the maximum illuminance of $\sim 15.000 \text{ lux}$ (Fig. 4f) and a maximum luminous efficacy (Fig. 4g) of $\sim 24 \text{ lumen/watt}$ and max EQE of 5.6% (Fig. 4g), showing that the obtained results are comparable to spin coated HTL and EIL and superior to evaporated calcium ($\sim 20 \text{ lumen/watt}$)⁵².

Buoyed by the superior OLEDs built by SoS, large area ($5 \times 5 \text{ cm}^2$ substrate) OLEDs are built. Since the ultrathin layer used in the OLEDs architecture is EIL, and should be deposited over the heat sensitive low surface energy layer SY, in here the EIL was deposited by the SoS method and other organic layers are built by spin coating. The J-V behaviour of these large area devices (Fig. 4h) is as good as small area devices (Fig. 4f) showing the uniformity in the charge injection behaviour. The inset of Fig. 4h clearly shows the homogenous illumination in the large area device, where the supplementary vide S3 shows the illumination behaviour of the small and large area devices over various applied potentials. The culmination of the theoretical and experimental

explanation to produce an ultrathin film of various materials with a highly efficient large area application of OLEDs indicates the credentials of the SoS technology to be used in many large area ultrathin layer applications.

Conclusion

The novel Spray-on-Screen technology inspired by the eyelids and the legs of water striders made it possible to convert the microdroplets from USSC into milli-droplets on the screen mesh. Based on the spectrum of the surface tension of the liquid being used, the wetting of the screen is explained by the models given by Wenzel and Cassie Baxter. This is followed by transferring the milli-droplets from the screen mesh to the substrate upon the application of an external force on the mesh. A capillary force exists between the substrate and the milli-droplets facilitating the spreading of the liquid over the substrate with the assistance of the force applied by the mesh. The presence of the screen mesh induces dynamic wetting and hence limiting the scope for contact line pinning. The experimental results achieved by the deposition with the SoS technology of PEDOT:PSS, PEIE and a ZnO-PEIE composite exhibit a thickness of the deposited films which could be easily controlled by the varying solution concentration, resulting in a minimum thickness of 15.8nm, 4.8nm and 15.3nm respectively. This shows the versatility of the novel Spray-on-Screen coating to deposit ultra-low thin coatings from various materials. This is achieved irrespective of the kind of solvent and the substrate size and type (ITO or SY) being used. The thickness could be tailor-made over a wide area of depositions with very smooth layers (1.1nm, 0.3nm and 2.6nm respectively for PEDOT:PSS, PEIE and ZnO-PEIE composite films on super yellow substrates) opening up a new fabrication method for a wide range of application areas. By combining the microdroplet generation from USSC and the dynamic wetting by applying an external force on a screen mesh, ultra-thin coatings over a large area could be achieved. This nature-inspired, novel technology outperforms spin coating on the size of the substrate, outperforms other solution processing technologies for the thickness and roughness of the applied coating and outperforms vacuum deposition in view of the ease and cost of the process. Therefore, SoS is a promising technology for the deposition of ultra-thin coatings (< 15nm) on large areas, especially on heat-sensitive substrates for a variety of applications. The suitability of the SoS to build thin films for a potential application is shown by building small area OLEDs with both PEDOT:PSS and ZnO-PEIE nanocomposite with SoS. The devices outperformed the evaporated devices and equal the spin coated devices. This shows the possibility of building highly efficient devices with SoS and also the large area devices built by SoS exhibit uniform illumination with the same J-V behaviour as that of small area devices showing the uniformity in the thickness which controls the charge injection. Therefore, among many, organic electronics (such as OLEDs, tandem solar cells) and battery research are the frontrunners in adopting the SoS in the near future.

Materials And Methods

Materials

ITO coated glass substrates were purchased from BIOTAIN Hongkong co. limited (thickness of $135\text{nm} \pm 5\text{nm}$, with a resistance of $10 \sim 15 \Omega\text{q}^{-1}$ with a transmittance of > 85%). poly(3,4-ethylenedioxythiophene) polystyrene sulfonate (PEDOT:PSS, grade Al 4083) were purchased from Heraeus. Super yellow light emitting

PPV copolymer (SY), Polyethylenimine, 80% ethoxylated solution (PEIE, 37% wt % in H₂O), Zinc oxide nanoparticle ink with a particle diameter of 10-15nm dispersed in IPA were purchased from Aldrich.

All the samples are cleaned according to the following protocol: ultrasonication-30 min in soap water, 20 min in demineralized water, 10 min in acetone and 10 min in isopropanol alcohol. Then the samples are dried with nitrogen gas. Finally, all the samples are UV-Ozone treated for 30 min.

Thin film fabrication

An ultrasonic spray coater from Sono-Tek corporation, equipped with an impact nozzle was used to spray coat. A programmable 25 ml syringe pump as a reservoir for the materials of interest, which is connected to the atomizing nozzle by tubing. The USSC nozzle was actuated at 120 kHz frequency at a generator power of 3 W. For all the set of experiments, a path speed of 10 mm s⁻¹, nitrogen shroud pressure of 1.5 kPa above the atmosphere is maintained. The polyester screen from Mediascreen is first cleaned by water then followed by IPA. Then the mesh is dried by using nitrogen gas for 2 min.

Characterization

The surface morphology and the thickness of the thin films were measured using a JPK-Bruker Atomic force microscope (AFM) with atomic resolution less than 0.030 nm and ultra-low noise level of cantilever deflection detection system which is less than 2 pm RMS; silicon ACTA tips on AC mode in the air with cantilever length 125 µm, spring constant 40 Nm⁻¹, and resonance frequency 300 kHz were used. Force Spectroscopy was performed by using an Au-coated tip (**Figure S13**) which was calibrated using a clean ultra-flat gold substrate (**Figure S14**). On each region of 10 µm², a grid of 100 points was set and force curves were taken at each of those points applying 2 nN. Young's modulus was calculated using the data processing software of the AFM applying the Hertz/Snedon model. All measurements were carried out in contact mode in air. Scanning electron microscopy (SEM) images were recorded by using Zeiss 450 gemini 2 FEG-SEM. Contact angle measurements were conducted by using Data physics OCA 15 Plus and the results were visualized and analysed using SCA 20 software. Zeiss Axiovert 40 MAT, inverted microscopy along with Zeiss AxioCam 305 colour are utilised for the optical microscopy images.

References And Notes

1. Liu, X., Xu, Y. & Chu, P. K. Preparation, Characterization, and Potential Biomedical Applications of Nanostructured Zirconia Coatings and Films. *Nanotechnologies Life Sci.* **5**, 251–275 (2011).
2. Manish Chhowalla & Gehan A. J. Amaratunga. Thin films of fullerene-like MoS₂ nanoparticles with ultra-low friction and wear. *Nature* **407**, 164–167 (2000).
3. Ding, D. *et al.* Interface Engineering in Solution-Processed Nanocrystal Thin Films for Improved Thermoelectric Performance. *Advanced Materials* vol. 29 (2017).
4. Chopra, K. L., Paulson, P. D. & Dutta, V. Thin-film solar cells: An overview. *Prog. Photovoltaics Res. Appl.* **12**, 69–92 (2004).
5. Windisch, R. *et al.* 40% Efficient Thin-Film Surface-Textured Light-Emitting Diodes By Optimization of Natural Lithography. *IEEE Trans. Electron Devices* **47**, 1492–1498 (2000).

6. Postica, V. *et al.* Improved Long-Term Stability and Reduced Humidity Effect in Gas Sensing: SiO₂ Ultra-Thin Layered ZnO Columnar Films. *Advanced Materials Technologies* (2021)
doi:10.1002/admt.202001137.
7. Soumah, L. *et al.* Ultra-low damping insulating magnetic thin films get perpendicular. *Nat. Commun.* **9**, 1–6 (2018).
8. Hu, D. *et al.* Ultra-sensitive nanometric flat laser prints for binocular stereoscopic image. *Nat. Commun.* **12**, (2021).
9. Wan, J. *et al.* Ultra-thin solid electrolyte interphase evolution and wrinkling processes in molybdenum disulfide-based lithium-ion batteries. *Nat. Commun.* **10**, 1–10 (2019).
10. Ma, J. *et al.* Giant energy density and high efficiency achieved in bismuth ferrite-based film capacitors via domain engineering. *Nat. Commun.* **9**, (2018).
11. Koller, L. R. Physical Properties of Thin Metallic Films. III. Some Factors Affecting the Resistance of Sputtered Platinum Films. *Phys. Rev.* **18**, 221–235 (1921).
12. Ugust, A. Photoelectric p r o p e r t i e s of zinc single crystals. **349**, 408–415 (1931).
13. Unvala, B. A., Woodcock, J. M. & Holt, D. B. Epitaxial growth of cubic ZnS by evaporation in ultra-high vacuum. *J. Phys. D. Appl. Phys.* **1**, 11–14 (1968).
14. Lim, B. S., Rahtu, A. & Gordon, R. G. Atomic layer deposition of transition metals. *Nat. Mater.* **2**, 749–754 (2003).
15. Cho, A. Y. & Arthur, J. R. Molecular beam epitaxy. *Prog. Solid State Chem.* **10**, 157–191 (1975).
16. Campbell, S. A. & Smith, R. C. Chemical vapour deposition. *High-K Gate Dielectr.* 65–88 (2003)
doi:10.1016/b978-012524975-1/50009-4.
17. Washo, B. D. Rheology and Modeling of the Spin Coating Process. *IBM J. Res. Dev.* **21**, 190–198 (1977).
18. Yan, L., Song, Y., Zhou, Y., Song, B. & Li, Y. Effect of PEI cathode interlayer on work function and interface resistance of ITO electrode in the inverted polymer solar cells. *Org. Electron.* **17**, 94–101 (2015).
19. Salles, P. *et al.* Electrochromic Effect in Titanium Carbide MXene Thin Films Produced by Dip-Coating. *Adv. Funct. Mater.* **29**, 1–9 (2019).
20. Padrón-Hernández, W. Y. *et al.* Stable inks for inkjet printing of TiO₂ thin films. *Mater. Sci. Semicond. Process.* **81**, 75–81 (2018).
21. Singh, A., Gupta, S. K. & Garg, A. Inkjet printing of NiO films and integration as hole transporting layers in polymer solar cells. *Sci. Rep.* **7**, 1–12 (2017).
22. Verma, A. *et al.* Towards industrialization of perovskite solar cells using slot die coating. *J. Mater. Chem. C* **8**, 6124–6135 (2020).
23. Kumar, S., Kim, H., Kim, D. kee & Iyer, S. S. K. Spin and doctor-blade coated PEDOT:PSS back electrodes in inverted organic solar cells. *Sol. Energy* **204**, 64–70 (2020).
24. Fasolt, B., Hodgins, M., Rizzello, G. & Seelecke, S. Effect of screen printing parameters on sensor and actuator performance of dielectric elastomer (DE) membranes. *Sensors Actuators, A Phys.* **265**, 10–19 (2017).
25. Zabihi, F., Xie, Y., Gao, S. & Eslamian, M. Morphology, conductivity, and wetting characteristics of PEDOT:PSS thin films deposited by spin and spray coating. *Appl. Surf. Sci.* **338**, 163–177 (2015).

26. Dundar, I., Mere, A., Mikli, V., Krunks, M. & Acik, I. O. Thickness effect on photocatalytic activity of tio₂ thin films fabricated by ultrasonic spray pyrolysis. *Catalysts* **10**, 1–13 (2020).
27. Bose, S., Keller, S. S., Alstrøm, T. S., Boisen, A. & Almdal, K. Process optimization of ultrasonic spray coating of polymer films. *Langmuir* **29**, 6911–6919 (2013).
28. Deegan, R. D. *et al.* Capillary flow as the cause of ring stains from dried liquid drops. *Nature* **389**, 827–829 (1997).
29. Pucci, M. F., Duchemin, B., Gomina, M. & Bréard, J. Dynamic Wetting of Molten Polymers on Cellulosic Substrates: Model Prediction for Total and Partial Wetting. *Frontiers in Materials* vol. 7 (2020).
30. Honnery, D., Nguyen, D. & Soria, J. Microdroplet evaporation under increasing temperature conditions: Experiments and modelling. *Fuel* **105**, 247–257 (2013).
31. Rowan, S. M., Newton, M. I. & McHale, G. Evaporation of microdroplets and the wetting of solid surfaces. *J. Phys. Chem.* **99**, 13268–13271 (1995).
32. Bush, J. W. M. & Hu, D. L. Walking on water: Biocomotion at the interface. *Annu. Rev. Fluid Mech.* **38**, 339–369 (2006).
33. Yang, E., Son, J. H., Lee, S. I., Jablonski, P. G. & Kim, H. Y. Water striders adjust leg movement speed to optimize takeoff velocity for their morphology. *Nat. Commun.* **7**, 1–9 (2016).
34. Baek, M. *et al.* Water strider females use individual experience to adjust jumping behaviour to their weight within physical constraints of water surface tension. *Sci. Rep.* **10**, 1–12 (2020).
35. Xuefeng, G. & Lei, J. Water-repellent legs of water striders. *Nature* **432**, 2004–2004 (2004).
36. Jung, Y. C. & Bhushan, B. Dynamic effects of bouncing water droplets on superhydrophobic surfaces. *Langmuir* **24**, 6262–6269 (2008).
37. Marmur, A. Wetting on hydrophobic rough surfaces: To be heterogeneous or not to be? *Langmuir* **19**, 8343–8348 (2003).
38. Verding, P., Deferme, W. & Steffen, W. Velocity and size measurement of droplets from an ultrasonic spray coater using Photon Correlation Spectroscopy and Turbidimetry. *arXiv* **59**, 7496–7503 (2020).
39. Wolf, R. & Sparavigna, A. C. Role of Plasma Surface Treatments on Wetting and Adhesion. *Engineering* **02**, 397–402 (2010).
40. Cassie, B. D. Of porous surfaces,. 546–551 (1944).
41. CASSIE, A. B. D. & BAXTER, S. Large Contact Angles of Plant and Animal Surfaces. *Nature* **155**, 21–22 (1945).
42. Breitenbach, J. *et al.* *Droplet Wetting and Evaporation Droplet Wetting and Evaporation Edited by. Advances in Colloid and Interface Science* vol. 59 (2018).
43. Lafuma, A. & Quéré, D. Superhydrophobic states. *Nat. Mater.* **2**, 457–460 (2003).
44. Wenzel, R. N. Resistance of solid surfaces to wetting by water. *Ind. Eng. Chem.* **28**, 988–994 (1936).
45. BAXTER, S. Wetting and Contact-Angle Hysteresis. *Nature* **165**, 198–198 (1950).
46. Kim, J. Y., Cho, K., Ryu, S. A., Kim, S. Y. & Weon, B. M. Crack formation and prevention in colloidal drops. *Sci. Rep.* **5**, 1–9 (2015).
47. Butt, H. J. & Kappl, M. Normal capillary forces. *Adv. Colloid Interface Sci.* **146**, 48–60 (2009).

48. Fowkes, F. M. ATTRACTIVE FORCES AT INTERFACES. *Ind. Eng. Chem.* **56**, 40–52 (1964).
49. Ton-That, C., Shard, A. G. & Bradley, R. H. Thickness of spin-cast polymer thin films determined by angle-resolved XPS and AFM tip-scratch methods. *Langmuir* **16**, 2281–2284 (2000).
50. Shiratori, S. & Kubokawa, T. Double-peaked edge-bead in drying film of solvent-resin mixtures. *Phys. Fluids* **27**, (2015).
51. Mori, Y. H., van de Ven, T. G. M. & Mason, S. G. Resistance to spreading of liquids by sharp edged microsteps. *Colloids and Surfaces* **4**, 1–15 (1982).
52. Gilissen, K., Stryckers, J., Manca, J. & Deferme, W. Towards fully spray coated organic light emitting devices. *Org. Light Emit. Mater. Devices XVIII* **9183**, 918311 (2014).

Figures

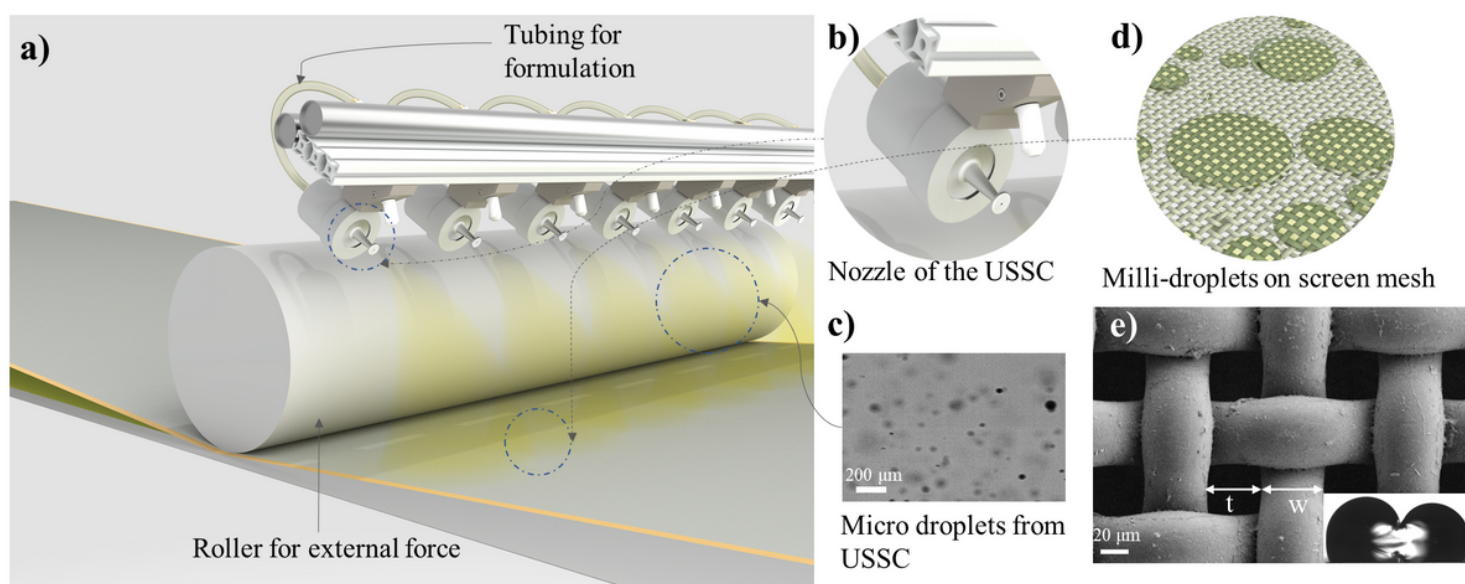


Figure 1

(a) Graphical abstract of the complete spray on screen technology **(b)** Schematic of the nozzle used in the USSC, **(c)** High-speed camera image of the generated droplets from the USSC, showing a droplet diameter distribution of 15 μm to 90 μm Video of the droplets generated from the USSC is shown in (movie S1)³⁸, **(d)** Graphical illustration of conversion of microdroplets into milli droplets on the screen mesh, **(e)** Scanning electron microscopy image for the screen used in the present study, with t = thickness of the thread (~ 50 μm) and w = opening of the mesh (~ 40 μm), inset, shows the hydrophobic thread cutting the water without piercing the same, and resembles the tiny legs of water striders.

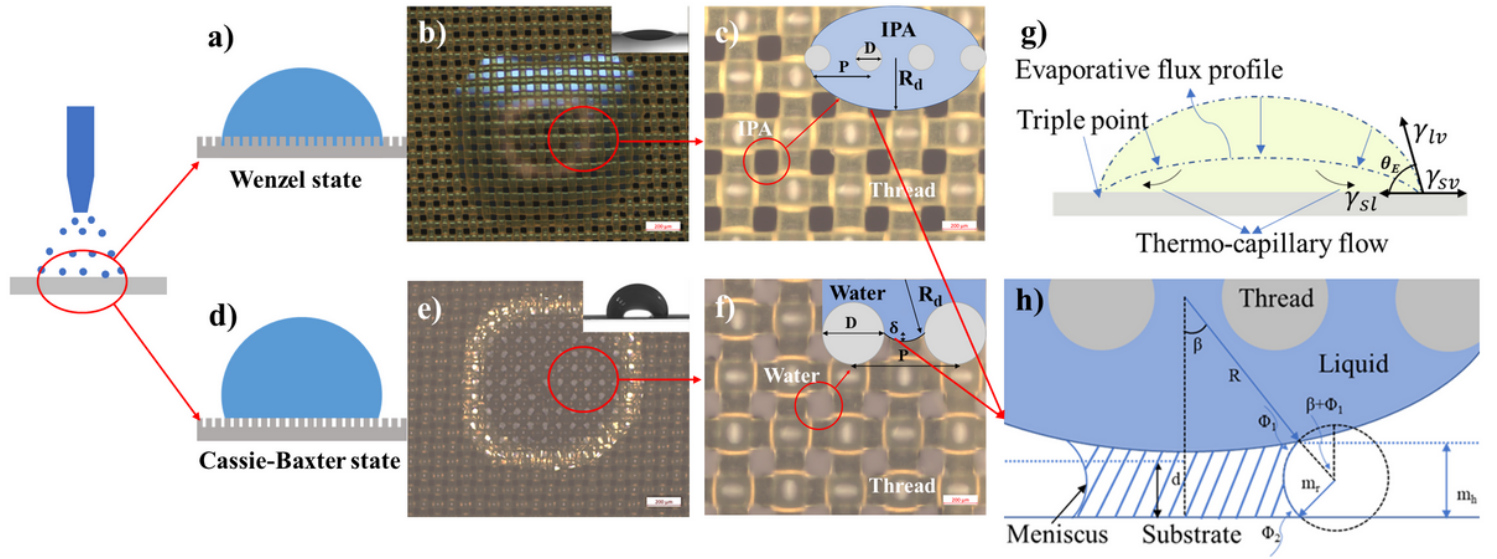


Figure 2

Droplet behaviour on the mesh. **(a)** Liquid wetting an idealized rough surface with Wenzel state, **(b)** optical microscope image taken at the rear end of mesh showing the behaviour of low surface tension liquid-like Isopropanol alcohol over the mesh and the top right inset shows the IPA exhibiting Wenzel state of wetting, **(c)** IPA over the mesh showing the formation of curved profile on top as well as the bottom of the mesh, resulting in the complete drooping of IPA below the mesh. **(d)** Liquid wetting an idealized rough surface with Cassie-Baxter state, **(e)** optical microscope image taken at the rear end of mesh showing the behaviour of high surface tension solvent like water exhibiting Cassie-Baxter state of wetting on micro-mesh (inset top right), **(f)** Partial drooping of water with a meniscus profile of the water between the threads of the mesh with a definite contact line. **(g)** Force balance at the triple junction between a liquid drop and flat substrate⁴⁵ and profile of the deposited droplet, with an equilibrium contact angle (θ), triple point, and also the evaporative flux profile⁴⁶ **(h)** Drooped liquid with radius R_d interacting with the substrate forming meniscus of radius m_r , the height of the meniscus is m_h , filling angle is β , Φ_1 and Φ_2 are the contact angle of the liquid meniscus with the drooped liquid and with the substrate, d is the distance between the drooped liquid and substrate.

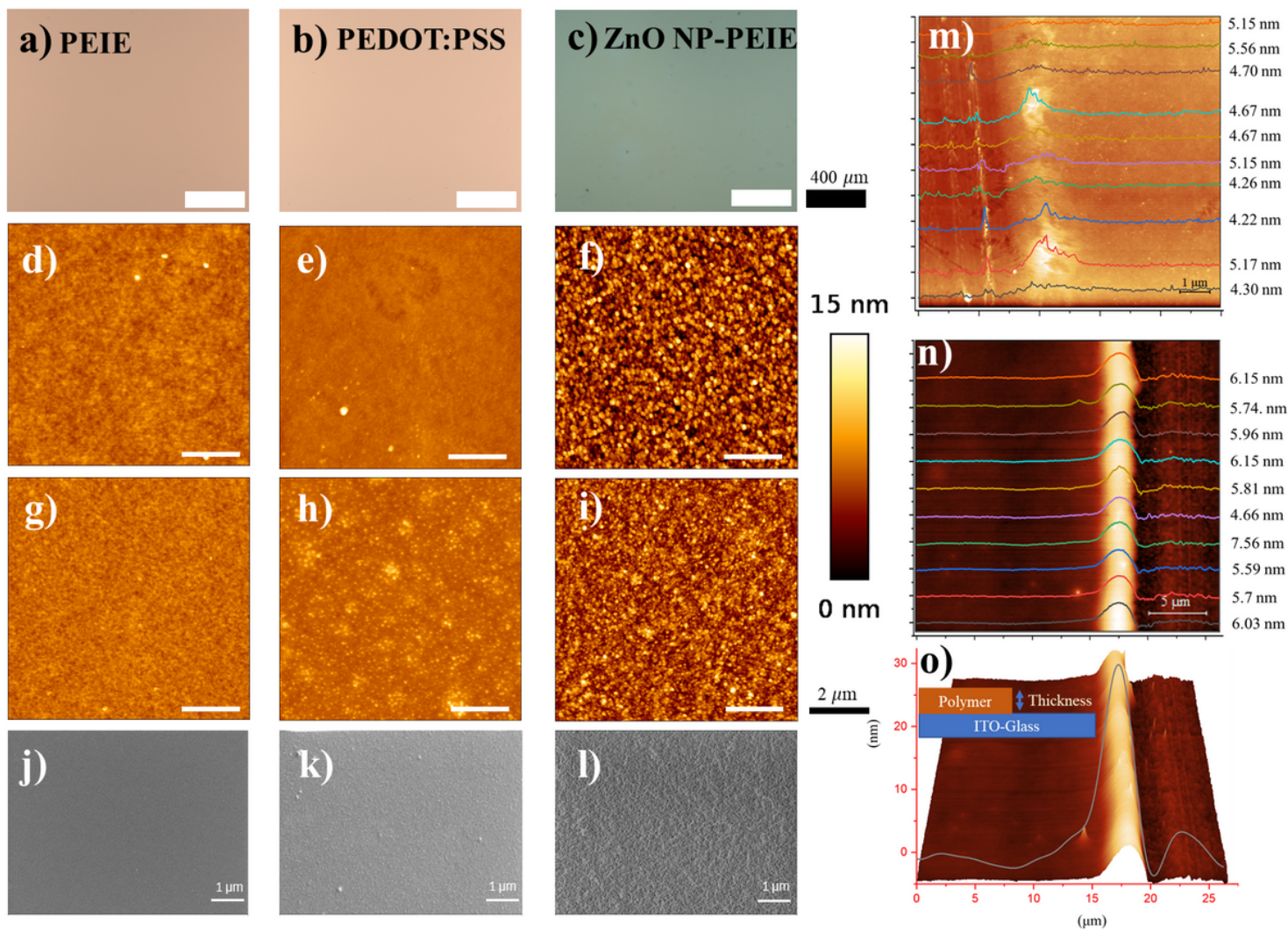


Figure 3

(a)(b)(c) Optical microscopy image, (d)(e)(f) Atomic force microscopy for the PEDOT:PSS, PEIE and ZnO-PEIE composite deposited on ITO substrate. Atomic force microscopy (g),(h) and (i) and scanning electron microscopy (j)(k) and (l) for the thin films of PEDOT:PSS, PEIE and ZnO-PEIE composite over the super yellow substrate. The sequence of the thickness measured for the spray on screen deposited PEIE on small and large samples are shown in (g) and (n) respectively. (o) 3-D image from the AFM showing the thickness measured on a trench created by scratching the polymer deposited on the ITO coated glass substrate, inset graphical representation of the scratch measurement.

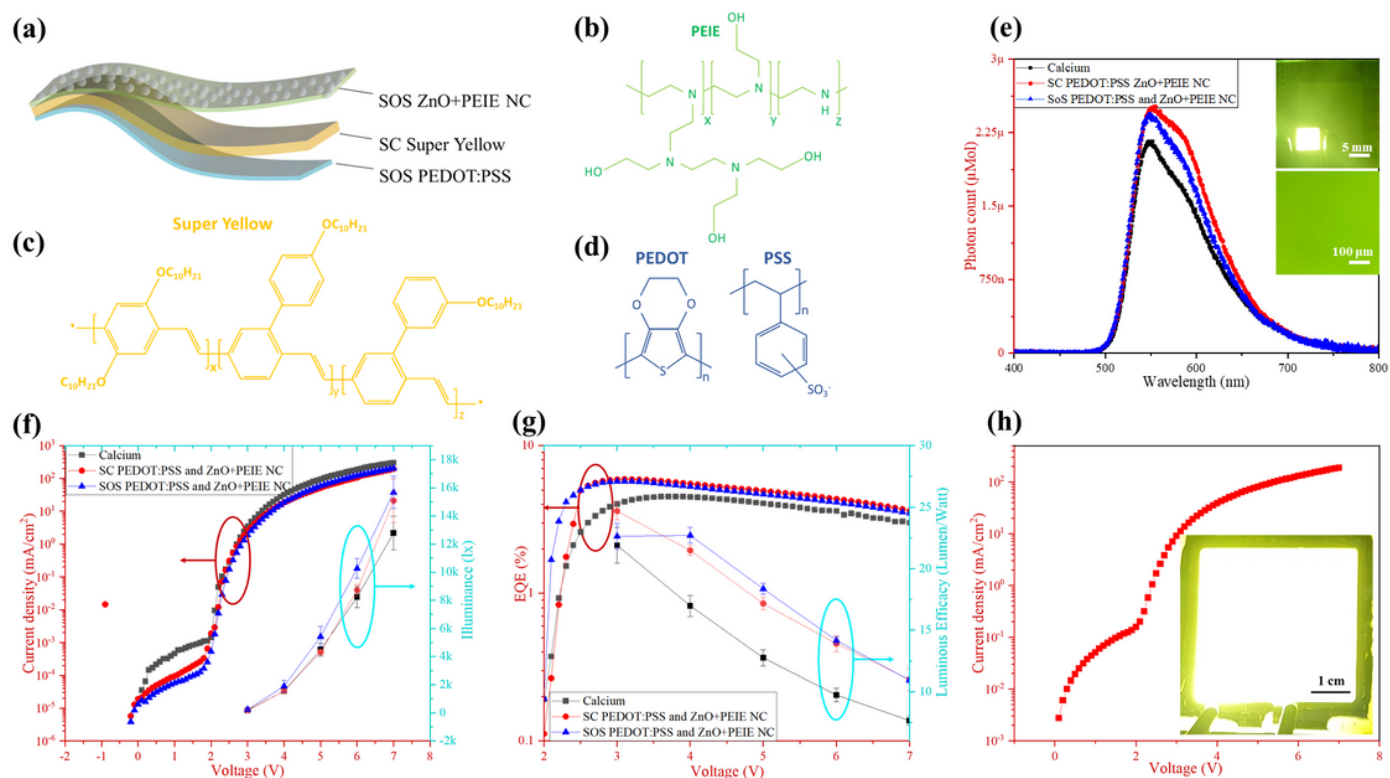


Figure 4

Performance comparison of the organic light emitting diodes (OLEDs) built by state of art standard devices with evaporated calcium, spin coated ZnO+PEIE nanocomposite and Spray on screen printed ZnO+PEIE nanocomposite as electron injection layer(EIL). (a) Solution processed organic semiconducting materials, PEDOT:PSS as hole transport layer(HTL), Super yellow(SY) as the active layer and ZnO+PEIE nanocomposite (NC) as electron injection layer. (b),(c) and (d) Chemical structure of the PEIE, SY and PEDOT:PSS respectively. (e) Electroluminescence behaviour of EIL built by different deposition methods, the top inset exhibits the illuminated small area OLEDs ($5 \times 5 \text{ mm}^2$), where HTL and EIL and is deposited by SOS technology, bottom inset showing the microscopic image showing the constant illumination. (f) Current density-voltage and illuminance (J-V-L) characteristics, (g) external quantum efficiency (EQE)-voltage and luminous efficacy characteristics of the small area OLEDs. (h) J-V characteristics for the large area OLEDs ($5 \times 5 \text{ cm}^2$ substrate), where the EIL is fabricated using the SoS method, bottom inset showing the homogeneous illumination of the large are OLEDs without any pinholes.

Supplementary Files

This is a list of supplementary files associated with this preprint. Click to download.

- [supplementaryinformationDepositionofultrathincoatingsbyanatureinspiredSprayonScreentechnology.docx](#)
- [slowmotionvideoofgeneratedmicrodropletsbyUSSC.mp4](#)
- [SoSworkingvideo.mp4](#)
- [RachithsprayonscreensmallandlargeareaOLEDnew.mov](#)